Cavity-Mediated Collective Emission from Few Emitters in a Diamond Membrane

Maximilian Pallmann,[1,*] Kerim Köster,[1,*] Yuan Zhang,[2,3,†] Julia Heupel,[4] Timon Eichhorn,[1] Cyril Popov,[4] Klaus Mølmer,[5] and David Hunger[1,6,‡]

[1]*Physikalisches Institut, Karlsruhe Institute of Technology (KIT), Wolfgang-Gaede Str. 1, 76131 Karlsruhe, Germany*
[2]*School of Physics and Microelectronics, Zhengzhou University, Zhengzhou 450052, China*
[3]*Institute of Quantum Materials and Physics, Henan Academy of Sciences, Zhengzhou 450046, China*
[4]*Institute of Nanostructure Technologies and Analytics (INA), Center for Interdisciplinary Nanostructure Science and Technology (CINSaT), University of Kassel, Heinrich-Plett-Straße 40, 34132 Kassel, Germany*
[5]*Niels Bohr Institute, University of Copenhagen, 2100 Copenhagen, Denmark*
[6]*Institute for Quantum Materials and Technologies (IQMT), Karlsruhe Institute of Technology (KIT), Herrmann-von-Helmholtz Platz 1, 76344 Eggenstein-Leopoldshafen, Germany*

(Received 10 November 2023; revised 2 September 2024; accepted 21 October 2024; published 4 December 2024; corrected 13 February 2025)

When an ensemble of quantum emitters couples to a common radiation field, their polarizations can synchronize and a collective emission termed superfluorescence can occur. Entering this regime in a free-space setting requires a large number of emitters with a high spatial density as well as coherent optical transitions with small inhomogeneity. Here, we show that, by coupling nitrogen-vacancy centers in a diamond membrane to a high-finesse microcavity, also few, incoherent, inhomogeneous, and spatially separated emitters—as are typical for solid state systems—can enter the regime of collective emission. We observe a superlinear power dependence of the emission rate as a hallmark of collective emission. Furthermore, we find simultaneous photon bunching and antibunching on different timescales in the second-order autocorrelation function, revealing cavity-induced interference in the quantized emission from about 15 emitters. We develop theoretical models for mesoscopic emitter numbers to analyze the behavior in the Dicke state basis and find that the population of collective states together with cavity enhancement and filtering can explain the observations. Such a system has prospects for the generation of multiphoton quantum states, the preparation of entanglement in few-emitter systems, and enhancement of signals in quantum sensing.

DOI: 10.1103/PhysRevX.14.041055

Subject Areas: Optics, Quantum Physics, Quantum Information

I. INTRODUCTION

Collective emission of quantum emitters is an intriguing behavior that can arise from the coupling of closely spaced atomic dipoles, where one of the most prominent features is a time-delayed superradiant pulse that grows quadratically in intensity with the emitter number [1]. It has been subject of numerous studies [2–9] and currently spurs great interest for possible applications, such as superradiant lasers [10,11], quantum memories [12–15], and quantum metrology [16].

Notably, even incoherent excitation can lead to spontaneous synchronization of emitters, an effect called superfluorescence [17,18]. This requires emitters with sufficient optical coherence and a high spatial density such that the average distance between two emitters is smaller than the transition wavelength. Reaching this regime can be challenging in a solid state environment, as emitters in dense ensembles typically suffer from effects like inhomogeneous and homogeneous broadening and spectral diffusion [19–21]. Recently, superfluorescence from perovskite quantum dot superlattices could be observed, which showed narrow ensemble emission lines under cryogenic conditions [8]. Surprisingly, also under strong phonon broadening at room temperature, high-density ensembles of nitrogen vacancy centers in nanodiamonds showed signatures of superfluorescence [22]. In both cases, a high density and a large number of emitters were crucial for the emergence of collective emission. These requirements can be relaxed by coupling the emission to a high-finesse microcavity, which acts as a single-mode common light

*These authors contributed equally to this work.
†Contact author: yzhuaudipc@163.com
‡Contact author: david.hunger@kit.edu

Published by the American Physical Society under the terms of the Creative Commons Attribution 4.0 International license. Further distribution of this work must maintain attribution to the author(s) and the published article's title, journal citation, and DOI.

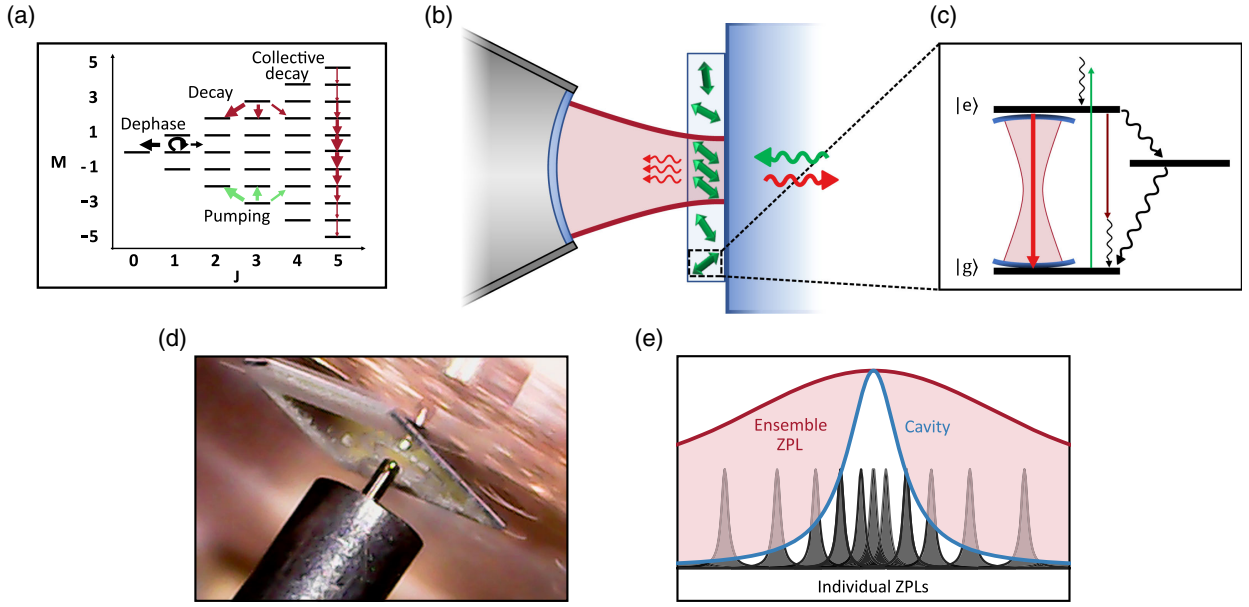

FIG. 1. Experimental setup and involved physics. (a) Exemplary level scheme of collective Dicke states for ten identical two-level emitters where the quantum jumps due to the incoherent pumping (green arrows), dephasing (black arrows), and individual and collective decay (red arrows) are indicated. (b) An NV center ensemble in a diamond membrane coupled to a fiber-based microcavity, where the NV centers are excited incoherently and emit collectively. (c) Simplified level scheme of the NV center. The ZPL $|g\rangle \leftrightarrow |e\rangle$ is resonant with the cavity, leading to selective Purcell enhancement of the transition. The system is excited off resonance via the phonon sideband (green arrow). (d) Photograph of the cavity setup, showing the fiber micromirror mounted in a steel needle and the diamond membrane on a planar mirror. (e) Schematic drawing of the inhomogeneously broadened ensemble ZPL, consisting of many individual transitions from which a few are overlapping with the narrow cavity resonance.

field that can couple also distant emitters and provides full spatial coherence [23,24]. Furthermore, the spontaneous emission rate is increased due to the Purcell effect [25], and photons are funneled into a spectrally narrow cavity resonance [26], which improves their spectral coherence.

In an idealized picture, a system of N identical emitters can be described in a basis of collective Dicke states $|J, M\rangle$ analogous to a number of spin $1/2$ systems that form a collective spin $J = 0, 1/2 \ldots N/2$ with a projection $M = -J \ldots J$ that represents the overall number of excitations $J + M$. As shown in Fig. 1(a), the collective decay preserves J and leads to quantum jumps between states with different M, while dephasing and individual decay cause quantum jumps also to states with different J. The relative rates of the jumps are illustrated by the thickness of the arrows, and their precise values can be found in Refs. [27,28]. Overall, dephasing tends to reduce J and lead to the population of subradiant states close to the lower boundary of the triangle. Because of their suppressed collective coupling to the cavity mode, these states promote excitation to higher levels under continuous pumping. These, in turn, can decay via the emission of multiple photons, leading to photon bunching [23,29]; see Fig. 1(a). This has been observed for ultracold atoms [30] and for larger numbers of solid state emitters [8,22,31,32].

Here, we report the observation of collective emission from a small ensemble of nitrogen-vacancy (NV) centers in diamond which display inhomogeneous and homogeneous broadening. They are dispersed over a few-micron large area in a diamond membrane and are resonantly coupled to a microcavity; see Fig. 1(b). Remarkably, for such sample properties, we observe a superlinear increase of the emission rate with increasing incoherent excitation, indicating the onset of collective emission. On the other hand, we observe the hallmark of quantized emission of individual emitters with antibunching in the second-order correlation function. Furthermore, on a short timescale, we observe a sharp bunching peak. Notably, all these features are solely visible for the coherent zero-phonon-line (ZPL) photons at low temperature, while they are absent for the incoherent phonon sideband (PSB) and at room temperature. To analyze the findings, we develop two complementary theoretical models that can treat the radiation of mesoscopic emitter numbers coupled to a cavity. Thereby, we can reproduce the observations and obtain a detailed insight into the contribution of the population of collective Dicke states and the influence of the emitter number, dephasing, and inhomogeneity.

II. CAVITY-ENHANCED FLUORESCENCE

We incorporate NV centers in a thin membrane into a fully tunable, fiber-based microcavity with a quality factor of $Q = 4.7 \times 10^5$ at the wavelength of the ZPL of the NV

centers; see Figs. 1(b)–1(d). The cavity linewidth is much narrower than the inhomogeneously broadened ZPL of the ensemble [Fig. 1(e)], such that a small number of resonantly coupling NV centers is spectrally selected. These emitters couple with a Purcell-enhanced rate to a single cavity mode.

We study the cavity-enhanced fluorescence by recording photoluminescence (PL) spectra under off-resonant excitation. Therefore, the cavity fiber was laterally positioned such that the fundamental Gaussian mode shows an airlike character [33] at $\lambda = 637$ nm with a finesse of $\mathcal{F} = 12\,000$. When tuning a cavity resonance to the ZPL, the resulting spectrum shows a series of sharp cavity resonances, with a dominant line at the ZPL wavelength [Fig. 2(a)]. Within the spectrally broad phonon sideband, a large number of additional fundamental and higher-order transverse cavity modes is visible. The measurement also illustrates the improved ratio of ZPL and PSB photons, as compared to a confocal measurement at room temperature. This results from the Purcell effect, which leads to an increased emission rate and, thereby, an improved branching ratio, a higher emission directionality, leading to a better collection efficiency, and the suppression of off-resonant fluorescence by cavity spectral filtering. We remark that, while for the cavity-enhanced ZPL emission only about 15 emitters contribute due to spectral filtering, all emitters (approximately 500) spatially located within the cavity mode contribute to the resonances in the phonon sideband as shown below. Thus, the ZPL enhancement is, in fact, more than an order of magnitude larger than is visible in Fig. 2(a). By applying a stepwise increasing voltage to the z-piezo and, thus, controlling the cavity length, the cavity resonance is tuned across the ensemble ZPL; see Fig. 2(b). Since the spectral cavity linewidth of $\delta\nu_{\mathrm{cav}} = 1.0$ GHz is much narrower than the inhomogeneously broadened ZPL, we can obtain a high-resolution spectrum. The summed counts reveal the spectral distribution of ZPL transitions sitting on a broad PSB background yielding an estimate of the full width at half maximum (FWHM) of $\delta\nu_{\mathrm{inh}} \approx 300$ GHz. When the cavity resonance frequency matches the center frequency of the inhomogeneous ZPL distribution, where most individual ZPLs couple to the cavity, an up to fourfold increase of fluorescence counts can be observed due to the Purcell effect and the above-mentioned consequences.

In a next step, we measure the power dependence of the fluorescence spectra under off-resonant excitation and compare the partially coherent emission into the ZPL with the redshifted incoherent emission into the phonon side band. While the power dependence for the PSB emission matches the expected linear scaling when far from saturation, the trend for the ZPL emission clearly exhibits a superlinear behavior following a power-law dependence $I \sim P^k$ with an exponent as high as $k = 1.42$; see Fig. 2(c). This is reproducible under various conditions like different cavity length or lateral position on the sample [inset in Fig. 2(c)]. The superlinear behavior was observed only at cryogenic temperatures ($T = 11$ K), in accordance with the prediction from a theoretical model (see below and Supplemental Material [34]). For an ensemble of superradiant emitters, one expects up to $k = 2$. The lower value observed in the experiment can be explained by the inhomogeneity, excitation-induced spectral diffusion on short timescales, and pure dephasing of the emitters, which leads to a population of Dicke states toward low J values.

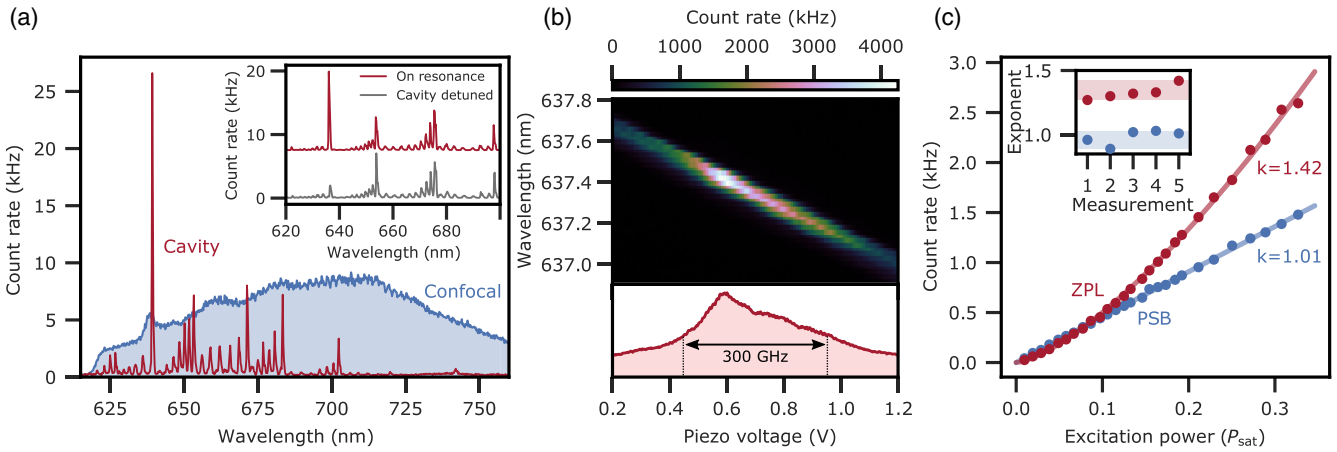

FIG. 2. Cavity-enhanced fluorescence of NV centers. (a) PL spectrum of an ensemble in the cavity (red) and in a confocal microscope (blue). The inset illustrates the decreased ZPL count rate as the cavity resonance is detuned from the transition by slightly changing the mirror separation. (b) Cavity-enhanced spectroscopy of the ensemble ZPL, obtained by recording fluorescence spectra while stepwise changing the cavity length. The integrated counts reveal the inhomogeneous ZPL with a FWHM linewidth of $\delta\nu_{\mathrm{inh}} \approx 300$ GHz. (c) Comparison of ZPL and PSB fluorescence count rates, coupled to the same spatial cavity mode, in dependence of the excitation laser power. The ZPL features a superlinear increase, a characteristic of superfluorescent emission. The inset shows exponents obtained under different conditions like cavity length or lateral position.

These states decay at a lower rate, which corresponds to a smaller value for k which is in detail evaluated below and in Supplemental Material [34].

III. PHOTON STATISTICS

Further insight can be obtained by studying the photon statistics of the radiation emitted from the cavity. Therefore, we use a Hanbury-Brown and Twiss (HBT) setup and record the second-order autocorrelation function $g^{(2)}(\tau)$. An exemplary $g^{(2)}(\tau)$ of the cavity-enhanced ZPL fluorescence is shown in Fig. 3(a), where three contributions can be fitted by the function

$$g^{(2)}(\tau) = 1 - (a+b)e^{-|\tau|/\tau_1} + be^{-|\tau|/\tau_2} + \phi_{c,\tau_3}(\tau). \quad (1)$$

Here, a and τ_1 (b and τ_2) describe the single-emitter antibunching (bunching) amplitude and time constant that are linked to the NV center excited (shelving) state lifetime, and $\phi_{c,\tau_3}(\tau)$ is the shelving state related bunching. We can extract the cavity-shortened excited state lifetime and, thus, the Purcell factor from the antibunching time constant $\tau_1(I)$, which depends on the excitation rate η and, thus, the laser intensity I. Therefore, we perform a power-dependent set of measurements of the $g^{(2)}$ function and evaluate $\tau_1(I)$; see Fig. 3(c). Extrapolating to zero

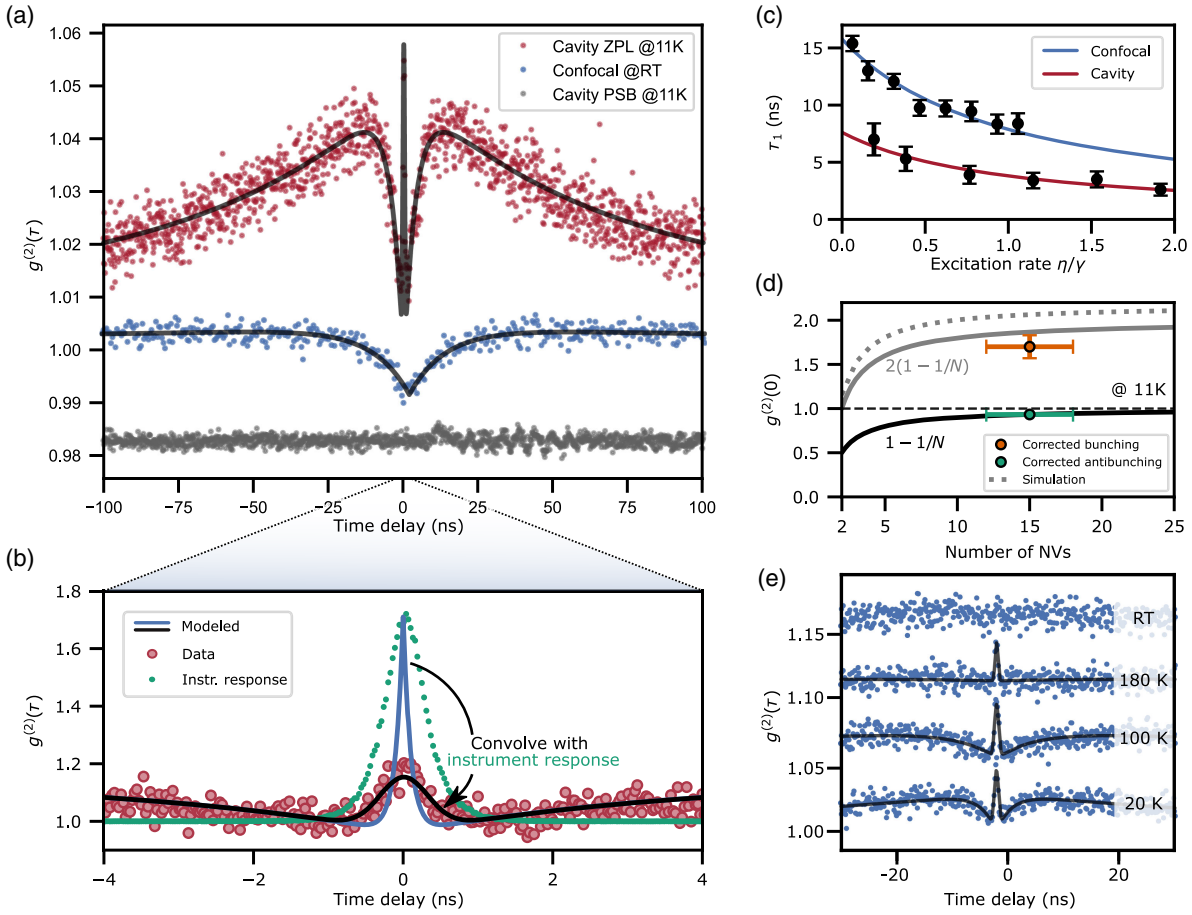

FIG. 3. Temporal photon statistics of NV fluorescence. (a) Second-order autocorrelation function of the emitted photons. The cavity-enhanced fluorescence (red data points) reveals bunching on a subnanosecond timescale, as opposed to the fluorescence recorded in a confocal microscope (blue data points). The PSB emission in the cavity setup (gray data points, shifted by 0.02 for clarity) does not show any bunching or antibunching. (b) Enlarged view of the bunching around $\tau = 0$ together with the measured instrument response function. A modeled $g^{(2)}(\tau)$ function is convolved with the instrument response to show the agreement with the background-corrected experimental data. (c) Antibunching time constants for different excitation laser intensities, extracted from the respective correlation functions. The fits correspond to a rate equation model and allow one to infer the effective Purcell factor $F_{\mathrm{P,eff}} = 1.1 \pm 0.3$. The error bars represent the standard deviation of the fit. (d) From the measured antibunching amplitude, one can extract the number of contributing emitters $N = 15 \pm 3$. For N individually decaying emitters, one expects a thermal bunching amplitude of $2(1-1/N)$ (solid gray line), which coarsely agrees with our measured value (orange data point). The prediction of our model is shown for comparison (dashed gray line). The horizontal (vertical) error bars represent the standard deviation of the respective $g^{(2)}$ fit rescaled by the purity (and instrument response) which is explained in more detail in the text. (e) A set of $g^{(2)}$ functions for increasing temperature reveals that the bunching amplitude is robust against further dephasing.

excitation intensity yields the excited state lifetime. The fit function $\tau_1(I) = \tau_1(0)/(1 + \sigma I \tau_1(0))$ can be deduced from simplified two-level rate equations, where $\sigma I = \eta$ is the excitation rate from the ground to the excited state with an experimentally determined proportionality factor σ (see Appendix B 3). With this analysis, the excited state lifetime of the cavity-coupled NV center ensemble was estimated as $\tau_c = \tau_1(0) = 7.6 \pm 0.9$ ns. A second set of power-dependent $g^{(2)}$ functions was taken in a confocal microscope, from which the excited state lifetime without cavity enhancement was estimated as $\tau_0 = 15.8 \pm 0.8$ ns. The increased lifetime compared to the bulk value of 13 ns can be explained by the presence of the nearby diamond-silica interface for shallowly implanted NV centers as studied here, which leads to a modified local dielectric environment that reduces the decay rate [35,36]. From the ratio of the cavity-enhanced and free-space lifetime, we can extract the effective Purcell factor to be $F_{\mathrm{P,eff}} = \tau_0/\tau_c - 1 = 1.1 \pm 0.3$, which corresponds to an ideal Purcell factor $F_{\mathrm{P,ideal}} = F_{\mathrm{P,eff}}/\zeta = 36 \pm 11$ with the Debye-Waller factor $\zeta = 0.03$ for NV centers [37]. This value is in the range of expected Purcell factors for the given cavity finesse, mode volume, dipole orientation, and random spectral cavity-emitter overlap and remains robust at different sample positions (see Appendix B 4). In general, a reduced excited state lifetime cannot solely be attributed to a single emitter Purcell effect in the presence of collective effects. However, in the studied regime with large dephasing and inhomogeneity, the collective decay is apparent only on very short timescales that do not overlap with the much longer antibunching timescale used to extract the lifetime. From the amplitude of the antibunching dip, we can deduce the number of emitters that couple to the cavity and, thus, dominantly contribute to the ZPL signal. Therefore, we follow the prediction for N independent emitters, which is given by $g^{(2)}(0) = 1 - 1/N = 1 - a$. In the presence of uncorrelated background, the antibunching contrast a is furthermore modified by the purity p such that $a/p^2 = 1/N$ applies. We define the purity as the fraction of the collected cavity radiation that originates from ZPL emission. Since a large number of spectrally detuned NV centers additionally contribute to the collected cavity resonance via their phonon sideband, they introduce uncorrelated background and, thus, reduce the purity. We can infer p by measuring the cavity-collected PSB background when detuning the cavity from the ensemble ZPL [see Fig. 2(b)] and obtain $p \approx 0.5$. In the case of the measurement shown in Fig. 3(a), this analysis yields $N = 15 \pm 3$ emitters coupling to the cavity. For comparison, we observe a flat $g^{(2)}$ function when selectively collecting the cavity-coupled PSB emission and an antibunching contrast of $a = 0.014$ in a measurement of the same sample region with a confocal microscope at room temperature. The latter contrast is smaller compared to the cavity ZPL measurement, since no spectral filtering is present and all excited emitters contribute. However, the spatial excitation and collection modes of the confocal microscope are smaller than the cavity mode cross section, such that fewer emitters are contributing than in the cavity under PSB collection. The antibunching contrast yields an estimate of hundred emitters in the confocal point-spread function and—scaled to the mode area of the cavity—about 500 emitters in the spatial cavity mode. This relatively high number explains why we do not observe any $g^{(2)}$ contrast in the cavity-filtered PSB.

We finally turn to the additional bunching peak close to zero time delay. We observe a Gaussian shape described with $\phi_{c,\tau_3}(\tau)$ in Eq. (1) with a FWHM of about 400 ps. This time constant is entirely limited by the instrument response of the HBT setup, originating from the timing jitter of the single photon count modules (SPCM). A measurement of the instrument response with a pulsed laser is shown in Fig. 3(b). In the limit of weak absorption, the fastest possible timescale for emission from the cavity is given by the cavity intensity decay time of $T_{\mathrm{cav}} = \delta\nu_{\mathrm{cav}}^{-1} = 100$ ps. This value is also in accordance with the developed model described below which considers emitters with additional dephasing that couple collectively to a cavity mode [see Figs. 4(c) and 4(d) and Supplemental Material [34]]. Correcting for the incoherent background from uncoupled NV centers and deconvolving the measured bunching peak allows us to estimate the intrinsic peak value of the bunching [Fig. 3(b)]. We obtain a value of $g^{(2)}(0) = 1.7$, which is close to an analytical estimate for interfering independent emitters [23,38], $g^{(2)}(0) = 2(1 - 1/N)$ for our extracted emitter number $N = 15 \pm 3$. This thermal limit describes individually decaying but identical emitters and neglects possible contributions from collective states. We compare the prediction for $g^{(2)}(0)$ from our theoretical model to the analytical expression in Fig. 3(d), and only a minor difference is visible. In contrast, no bunching is observed in the cavity-enhanced PSB at any temperature, as well as in the confocal measurement at room temperature.

Finally, to study the effect of dephasing more explicitly, we perform measurements of the $g^{(2)}$ function as a function of temperature [Fig. 3(e)]. We observe a decrease of the antibunching amplitude, in accordance with the prediction of our model when assuming a temperature-dependent dephasing rate as measured in Ref. [39]. We note that, at elevated temperature, also an increased number of emitters are expected to contribute to the signal. This is due to the increased homogeneous linewidth, which leads to a growing spectral overlap of detuned emitters with the cavity mode. The temperature-dependent collective bunching amplitude remains approximately constant, even when approaching room temperature. However, when accounting for the changing background contribution, an overall decrease results.

The measurements show that the collective bunching contrast is not very sensitive to collective effects in the presence of dephasing, and, e.g., superthermal

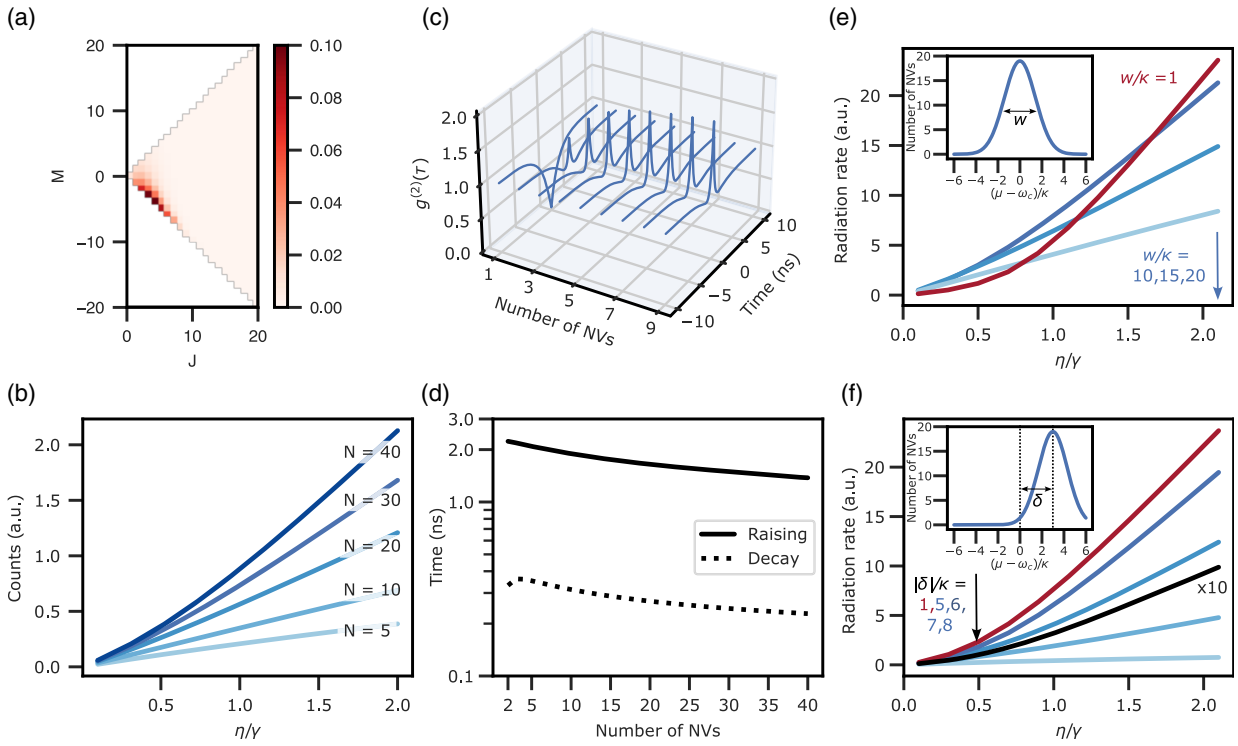

FIG. 4. Modeling of collective emission. (a)–(d) Results for an ensemble with identical NV centers. (a) Population of Dicke states under continuous incoherent pumping for 40 NV centers. While population peaks at the lower-left boundary of the triangle, also higher-lying collective states are populated. (b) Radiation rate as a function of the ratio η/γ between the pumping and decay rate, shown for an increasing number of NV centers N. (c) Second-order correlation function $g^{(2)}(\tau)$ for different values of N and $\eta/\gamma = 2$. (d) Corresponding decay and rise time of $g^{(2)}(\tau)$. (e),(f) Results for NV centers with different frequencies (subensembles). (e) Influence of a Gaussian distributed frequency inhomogeneity of 500 NV centers with a width w on the radiation rate. (f) Influence of the frequency detuning δ on the radiation rate, and the radiation weighted by the frequency fluctuation (black line, amplified by 10 times), treated by a Gaussian distribution of δ with a width 300 GHz.

bunching [23,32,40] is neither observed nor expected (see below). However, the observed signatures cannot be described solely by individually decaying emitters. In particular, due to the superlinear power dependence of the cavity emission and the differences between the ZPL and the PSB, the observations support the picture that the Purcell-enhanced emission into a single cavity mode synchronizes emission if strong enough cavity coupling and sufficient coherence are present.

IV. NUMERICAL MODEL

For a deeper analysis, we develop numerical models for small ensembles of emitters coupled to a cavity. We study first the case of identical NV centers to qualitatively explain the main physics [Figs. 4(a)–4(d)] and then introduce subensembles of NV centers with different transition frequencies to examine the influence of the frequency inhomogeneity and fluctuations [Figs. 4(e) and 4(f)]. For the sake of simplicity, we focus here on the transition between the $m_s = 0$ levels of the triplet states $^3A_2, ^3E$, because it dominates the radiation under continuous illumination. In our theoretical model (see Supplemental Material [34]), we treat this transition as a two-level system in the presence of decay, pure dephasing, incoherent pumping with rates γ, χ, and η. Here, the ratio η/γ is varied to model the power-dependent radiation rate, while χ is an estimate, chosen such that the numerical results are in agreement with the observations. The two-level system is coupled by a strength $g = 2\pi \cdot 180$ MHz to an optical cavity with frequency ω_c and a loss rate $\kappa = 2\pi \cdot 1.0$ GHz, both of which are experimentally determined parameters. All these processes are described by a quantum master equation (QME). For the homogeneous system, all the NV centers are identical, and they can be well described with Dicke states $|J, M\rangle$, and for a moderate emitter number, the QME can be solved in the basis of these states [27,28]. Under incoherent pumping with rate η, the excited ensemble emits radiation. Since our system is in the weak coupling regime, we can eliminate adiabatically the cavity to obtain the radiation rate $I_{\mathrm{rad}} = \Gamma \sum_{J,M} |A^-_{J,M}|^2 \rho^J_{MM}$, where $\Gamma \approx 4g^2/\kappa$ is the cavity-mediated Purcell-enhanced decay, the coefficient $A^-_{JM} = \sqrt{(J+M)(J-M+1)}$ arises from the action of the collective lowering operator, and ρ^J_{MM} is the total population of the degenerate Dicke

state manifold with the same quantum numbers J and M. As η increases, the steady state of the ensemble rises along the lower boundary of the Dicke states with decreasing values of J and $M = -J, -J+1, -J+2, \ldots$ [Fig. 4(a)], which leads to the increased radiation. Furthermore, as the number of NV centers increases, the number of excitations in the system increases, and the scaling of radiation changes from linear to superlinear [Fig. 4(b)]. We observe the onset of superlinear scaling for $N \gtrsim 15$, and, for $N = 40$, the scaling approximates the experimental findings, motivating the choice for N in Fig. 4(a). The difference in N compared to the experiment is expected, since this model neglects several aspects such as inhomogeneity that we address below. By applying the quantum regression theorem, we have also computed the second-order autocorrelation function $g^{(2)}(\tau)$. In general, this function does not change qualitatively with increasing pumping rate (see Supplemental Material [34]), and thus, here, we focus on the influence of the number of NV centers N for the pumping rate $\eta = 2\gamma$ in Fig. 4(c). While the $g^{(2)}(\tau)$ function shows a pronounced dip for a single NV center, it shows a sharp bunching peak around zero delay time $\tau = 0$ for $N \geq 2$ and an antibunching dip for longer time. The quantitative analysis of the time constants is illustrated in Fig. 4(d). The decay time of the peaks (the rising time of the dips) reduces to about 0.23 ns (1.37 ns) with increasing N. Note that the decay time increases slightly when N changes from 2 to 3. For $\eta = 2\gamma$ and $N = 40$, the Dicke states around $J = 4$ are populated, and the excited Dicke states with $M > J$ contribute to the radiation. We estimate the decay rate of the singly (doubly) excited state $|J = 4, M = -3(-2)\rangle$ as $\Gamma|A^{-}_{(4,-3)}|^2 = 8\Gamma$, $(\Gamma|A^{-}_{(4,-2)}|^2 = 18\Gamma)$, and find that the inverse of these rates $1/(8\Gamma) \approx 0.33$ ns and $1/(18\Gamma) \approx 0.15$ ns are close to the decay time 0.23 ns. The same applies also to the less populated Dicke states with $J \neq 4$. Since these values are close to the decay time 0.23 ns, the sharp antibunching peak of the $g^{(2)}(\tau)$ function should be associated with these excited Dicke states. When introducing additional dephasing at a value equal to the cavity decay rate, we observe a reduced bunching peak time constant of 110 ps which is rather insensitive to the emitter number and which closely matches the experimentally determined cavity decay rate of 100 ps (see Supplemental Material [34]). This motivates the choice of the time constant in the model for Fig. 3(b). At the same time, the peak maximum (dip minimum) increases and saturates gradually to a value slightly above 2 (below 1) for larger N. While the dip minimum matches closely with the analytical prediction, the bunching peak remains systematically higher than given by the analytical expression for independent emitters, reflecting the remnants of superthermal bunching for collective emission in the regime of incoherent emitters. The behavior is shown in Fig. 3(d) together with the experimental result, yielding good agreement. With the above results, we have confirmed that the nonlinear scaling and the sharp bunching peaks, as observed in the experiment, are caused by the cavity-mediated collective radiation of the NV centers. This is associated with the population of superradiant Dicke states, while strong superthermal bunching is not expected in the presence of significant dephasing.

To reflect more closely the experimental conditions, we study the influence of frequency inhomogeneity and fluctuations [41]. We divide the total NV centers into multiple subensembles with different frequencies and assume that their spectral distribution follows a Gaussian with a mean μ and a linewidth $w = 2\sqrt{2\ln(2)}\sigma$ (standard deviation σ). Although we cannot solve the QME of such a system with the density matrix technique due to the exponentially increased Hilbert space, we can solve it with the second-order mean-field theory and derive semianalytical expressions for the quantities characterizing the system steady state. In our simulations, we consider 500 NV centers, as estimated from the experimentally measured $g^{(2)}$ function. If the Gaussian distribution is resonant with the cavity and has a similar width $(\mu = \omega_c, w = \kappa)$, the radiation rate shows obvious superlinear and linear scaling for $\eta/\gamma \leq 1.2$ and $\eta/\gamma > 1.2$, respectively [Fig. 4(e)]. However, as w increases to 5κ, the superlinear scaling becomes less pronounced. If w increases further to 20κ, the radiation rate decreases and approaches gradually the linear scaling. If the Gaussian distribution with a fixed width $w = 3\kappa$ is detuned from the cavity by an increasing amount $\delta = \mu - \omega_c$, the radiation rate reduces slightly for smaller detuning $|\delta| \leq 3\kappa$ but dramatically for much larger detuning $|\delta| > 3\kappa$ [Fig. 4(f)]. Furthermore, by assuming that the probability of the detuning δ follows also a Gaussian distribution with a large linewidth $w \approx 300$ GHz, as estimated from Fig. 2(b), we can weigh the above results with this probability to obtain the averaged radiation [black line in Fig. 4(f)] and observe the persistence of the superlinear scaling.

To evaluate the influence of the frequency inhomogeneity and fluctuation on the $g^{(2)}$ function, we adopt an indirect approach and verify first that the radiation is affected by dephasing of NV centers in a similar way as by the frequency inhomogeneity (see Supplemental Material [34]), which permits us to account for the inhomogeneity in the model of identical NV centers with a single dephasing rate [42,43]. The sharp bunching peak of the g^2 function is preserved in the presence of large dephasing and frequency fluctuation. The models show that the central features of the experimental data can be reproduced qualitatively. An accurate quantitative simulation of the experiment would require a better knowledge of all involved dephasing and decay rates and to solve the QME for the entire ensemble, which is computationally prohibited by the exponential increase of the Hilbert space. In the end, we note that the observed bunching shoulder of the $g^{(2)}(\tau)$ function at

longer times is known to originate from the singlet excited levels $^1A_1, ^1E$ of NV centers, and, thus, improved models including also these levels should be able to capture all these characteristics. Because of the complexity of the models, we defer their discussion to a more detailed theoretical paper [44].

V. CONCLUSION

In summary, we demonstrate that incoherent, inhomogeneous, and spatially separated emitters can yield signatures of collective emission, enabled by the coupling to a common cavity mode. We have focused on the nonlinear scaling and the photon bunching of the incoherently pumped NV centers. It would be interesting to further explore the collective radiation from population-inverted NV centers or from a system with more NV centers, which might enter the strong coupling regime. Cavity-induced synchronization can furthermore lead to nontrivial collective behavior even for emitters outside the cavity linewidth [45]. Collective emission may be used to generate multiphoton quantum states [46] and can be a promising route to produce multiqubit entangled states [47,48]. Collective states can also enable improved sensitivity for quantum sensing [49,50]. It will be an intriguing direction to explore cooperative behavior in the cavity quantum electrodynamics regime that has recently been demonstrated for two emitters in cavities [51–55] and expand it to a controlled number of few emitters.

ACKNOWLEDGMENTS

We thank Florian Kaiser for helpful discussions and Jonathan Körber, Jeremias Resch, Evgenij Vasilenko, and Jonas Grammel for support in the early stage of the experiment. This work was partly supported by the German Federal Ministry of Education and Research (BMBF) within the project QR.X (Contracts No. 16KISQ004 and No. 16KISQ005), SPINNING (Contract No. 13N16211), the Carlsberg Foundation through the "Semper Ardens" Research Project QCooL, the Danish National Research Foundation through the Center of Excellence for Hybrid Quantum Networks (Grant Agreement No. DNRF139), the National Natural Science Foundation of China (Projects No. 12422413 and No. 62475242), the National Key R&D Program of China (Project No. 2024YFE0105200), the Karlsruhe School of Optics and Photonics (KSOP), and the Max-Planck School of Photonics (MPSP).

APPENDIX A: EXPERIMENTAL DETAILS

1. Diamond sample

The sample used in this experiment is an electronic-grade single-crystal CVD-grown diamond with a [100] surface orientation. The sample was initially cut to have an average thickness of 40 ± 10 μm and a thickness variation of <1 μm/mm. Afterward, the sample was shallowly implanted by the manufacturer (Qnami) with nitrogen ions, leading to a specified high density of NV centers (approximately 300 NV/μm^2) at a depth of 10 nm. The sample was further cut to have a footprint of 1.5×1.5 mm^2 and bonded onto a dielectric mirror by van der Waals bonding. Afterward, the diamond was machined by inductively coupled plasma reactive ion etching, creating a membrane with a minimal thickness of 3.5 μm and a surface roughness as low as 0.3 nm rms in an area of 4×4 μm^2 [56].

2. Microcavity platform

The setup used in this work consists of a home-built fiber-based microcavity platform that is integrated into a closed-cycle cryostat, cooling the sample down to 11 K, and an optical free-space collection and excitation path. The cavity platform is optimized to provide an extremely low passive stability at low temperatures with values as low as 2.4 pm rms, counteracting the noisy environment of the closed-cycle cryostat [57]. This is essential for our measurements, as we need the cavity to be on resonance with the NV ZPL for hours or even days, for some measurements.

The resonator itself is a plano-concave resonator formed with two distributed Bragg reflectors (DBRs), coated onto a macroscopic, superpolished fused-silica substrate on the one side and onto the end face of an optical fiber on the other side. The optical fiber has been machined using a CO_2 laser that imprints its lateral power profile onto the fiber by laser ablation [58]. The fiber mirror used here has a radius of curvature of 27.5 μm. The cavity length, given by the mirror distance, can be tuned using piezo actuators. Moreover, both the planar mirror as well as the fiber can be scanned laterally which is crucial to find a suitable spot on the sample. The coatings are designed to have 732 (52) ppm transmission on the macroscopic (fiber) mirror side at $\lambda = 637$ nm. The presence of the diamond with its high reflective index of $n_d = 2.41$, however, introduces an additional (partly) reflective surface to the planar side DBR and thereby alters its reflectivity, depending on the membrane thickness. There are two special cases: the "airlike" character, where the diamond thickness matches an integer multiple of $\lambda/2n_d$, and the "diamondlike" configuration, when the thickness is shifted by $\lambda/4n_d$. The resulting mirror transmission is then 236 ppm for the airlike and increased to 1370 ppm for the diamondlike case. In general, the operation using an airlike mode is desired, as some sources of loss located on the diamond-air interface like scattering or mode curvature mismatch are reduced or completely avoided [59]. On the fiber side, an additional reflection band is added around $\lambda = 532$ nm in order to avoid excitation light from entering the fiber which could cause unwanted fiber fluorescence.

3. Optical setup

We excite the NV centers incoherently using a continuous wave laser with $\lambda_{\mathrm{exc}} = 532$ nm (Cobolt Samba 100) through the free-space port of the cryostat. The same optical path is used to filter and collect fluorescence light. The transmitted light from the cavity is either collected directly using an avalanche photodiode (Thorlabs APD410A2/M) or coupled to the collection path with a flip mirror. In the collection path, the excitation light is filtered out by a dichroic mirror which is also used to overlap the excitation laser with the transmission beam path and an additional notch filter. The NV fluorescence is then recorded either with a spectrometer (Andor iVac 316 LDC-DD) or in a HBT setup, consisting of two single-photon counting modules (Excelitas SPCM-AQRH-12-TR, laser components COUNT-T100). For measurements in the HBT setup, the fluorescence light is filtered further to extract only the ZPL photons in the fundamental mode of the cavity. This is done using two bandpass filters that are spectrally shifted with respect to each other (Semrock FF01-637/7-25, Semrock SEM-TBP01-704/13). The second-order autocorrelation function is obtained using a time-to-digital converter (TimeTagger 20, Swabian Instruments).

APPENDIX B: COMPREHENSIVE EVALUATION

1. Number of emitters within a spatial and spectral cavity mode

In the simple case of a $g^{(2)}$ function without collective effects and without significant uncorrelated background [as is the case in the confocal measurement in Fig. 3(a)], the number of contributing emitters N relates directly to the antibunching contrast a via $a = 1/N$. The lowest antibunching contrast measured in the confocal microscope is $a = 0.014$ for a mode waist of $w_0 = 0.474$ μm. From the number of emitters and area of the confocal point spread function, we can deduce the density n of NV centers in the sample as $n \approx 100$ NV/μm^2. Using the cavity mode area, the number of emitters in the spatial cavity mode is $N_{\mathrm{inh}} \approx 500$. Additional spectral filtering by the cavity further reduces the number of emitters contributing to the ZPL signal significantly. This number can be determined by the antibunching contrast of the cavity-filtered fluorescence signal. However, the contrast must be adjusted for uncorrelated background, most of which comes from PSB contributions of underlying, inhomogeneously spread emitters. The measured $g^{(2)}(\tau)$ can be corrected to get the noise-free $g^{(2)}_{\mathrm{ZPL}}(\tau)$ via [60]

$$g^{(2)}(\tau) = 1 + \Delta y + p^2\left(g^{(2)}_{\mathrm{ZPL}}(\tau) - 1\right), \qquad \text{(B1)}$$

with the purity parameter $p = \mathrm{ZPL}/(\mathrm{ZPL} + \mathrm{PSB})$ and the y-axis offset Δy. In our case, the purity is $p \approx 0.5$, determined by the contrast between the on- and off-resonant count rate. This leads to a noise-free antibunching amplitude of 6.7%, corresponding to about 15 emitters that spectrally overlap with the cavity and, thus, substantially contribute to the signal. The purity as measured with SPCMs is significantly less compared to the spectrometer due to worse spectral filtering. Here, $p \approx 0.75$ has been achieved on the fundamental cavity mode.

The difference between the number of emitters in a spectral and a spatial cavity mode has a significant impact on the interpretation of the fluorescence spectrum shown in Fig. 2(a). Rescaling the PSB contribution of 500 down to 15 emitters would reveal the true ZPL enhancement.

2. Determining the purity

A critical parameter to evaluate the background-corrected antibunching amplitude and, thus, the number of contributing emitters is the purity $p = \mathrm{ZPL}/(\mathrm{ZPL}+\mathrm{PSB})$. We determine this parameter by sweeping the cavity resonance over the inhomogeneously broadened ZPL distribution and measuring the count rate on the detectors. An example count rate trace is shown in Fig. 5 with the corresponding ZPL and PSB count rates indicated. The background (PSB) is fitted by a linear curve. Here, the slope is a consequence of higher-order cavity modes spectrally moving into the bandpass-filtered detection window. The purity for the shown example count rate trace is evaluated to $p = 0.54$ but varied during all shown measurements by roughly 10% which is why this parameter is the largest source of uncertainty in the number of emitters, as it also enters quadratically into the $g^{(2)}$ antibunching contrast.

3. Power dependence of the antibunching time constant

In a simplified model of a two-level system (as shown in Fig. 6), we can write the population dynamics of state 1

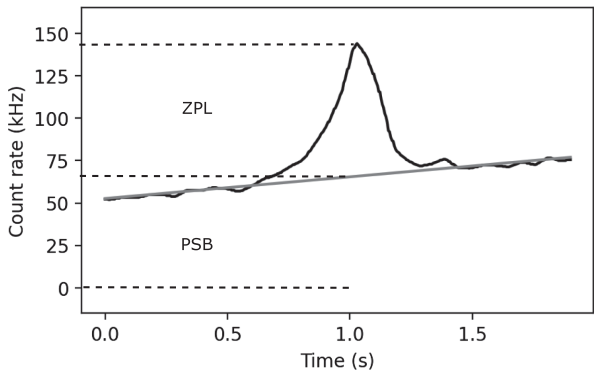

FIG. 5. Exemplary count rate trace on SPCMs. Here, one fundamental cavity resonance is swept over the inhomogeneously broadened ZPL.

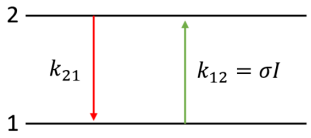

FIG. 6. Schematic of the involved rates in an off-resonantly driven two-level system.

(ground state) and state 2 (excited state) with a coupled differential equation:

$$\begin{pmatrix} \dot{\rho}_1 \\ \dot{\rho}_2 \end{pmatrix} = \begin{pmatrix} -k_{21} & k_{21} \\ k_{12} & -k_{21} \end{pmatrix} \begin{pmatrix} \rho_1 \\ \rho_2 \end{pmatrix}, \tag{B2}$$

where $k_{12} = \sigma \cdot I$ is the excitation rate which will be proportional to the applied laser intensity I and an experimental proportionality constant σ. The total population is constant: $\rho_1 + \rho_2 = 1$. Solving the differential equation for $\rho(t)$ yields the general result

$$\rho_2(t) = \frac{k_{12}}{k_{12} + k_{21}} + \alpha \cdot \mathrm{e}^{-t(k_{12}+k_{21})}. \tag{B3}$$

The $g^{(2)}(\tau)$ can be calculated from the excited state dynamics via $g^{(2)}(\tau) = \rho_2(\tau|1)/\rho_2^{\infty}$ [61]. Here, $\rho_2(\tau|1)$ is the excited state population starting in the ground state (detecting a click at $\tau = 0$), and $\rho_2^{\infty} = k_{12}/(k_{12} + k_{21})$ is the steady state population at $t = \infty$. Therefore, we can eliminate the integration constant α with $\rho_2(0) = 0$ to

$$\rho_2(t) = \rho_2^{\infty}\left(1 - \mathrm{e}^{-t(k_{12}+k_{21})}\right) \tag{B4}$$

and identify

$$g^{(2)}(\tau) = 1 - \mathrm{e}^{-t(k_{12}+k_{21})} = 1 - \mathrm{e}^{-t/\tau_1(I)}, \tag{B5}$$

with $\tau_1(I) = 1/(k_{12} + k_{21}) = \tau_1(0)/[1 + \sigma I \tau_1(0)]$ and $\tau_1(0) = 1/k_{21}$. Interpolating $\tau_1(I)$ to zero excitation intensity gives the excited state lifetime $1/k_{21}$.

4. Position dependence of the antibunching time constants

We measure $g^{(2)}$ functions at different sample positions in the confocal microscope as well as in the cavity, but not at the full extent as shown in Fig. 3(c). Two $g^{(2)}$ functions in the confocal microscope and in the cavity at two excitation rates show no significant deviation for τ_0 and τ_c as indicated by the four additional crosses in Fig. 7. In the case of the cavity measurement, the position is chosen such that the finesse is comparable to the measurements shown in the manuscript. This is crucial, because the finesse and, thus, the Purcell factor drastically vary due to the airlike or diamondlike variation over the entire sample.

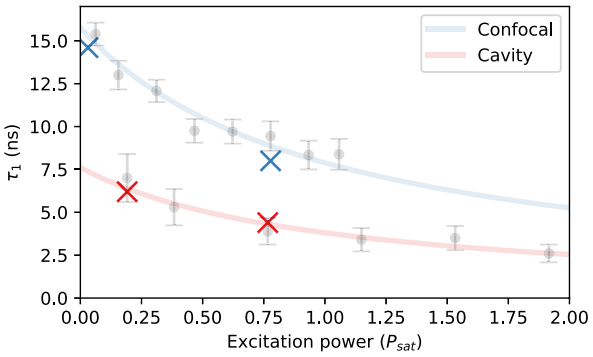

FIG. 7. Position-independent $g^{(2)}$ antibunching time constants. The added crosses are measured at different sample positions, and no significant deviations have been observed.

5. Expected Purcell factor

The Purcell factor $F_{\mathrm{P,ideal}} = 36 \pm 11$ is measured as a lifetime shortening by an excitation power-dependent set of $g^{(2)}$ functions. The expected Purcell factor is defined as the ratio of the cavity and free-space decay rate $F_{\mathrm{P}} = \gamma_c/\gamma_0$. The general derivation for the Purcell factor F_{P} can be found, e.g., in Ref. [62], of which we need only the final result

$$F_{\mathrm{P}} = \frac{3}{4\pi^2}\left(\frac{\lambda}{n}\right)^3 \frac{Q}{V_m} \cdot \xi = \frac{6}{\pi^3}\left(\frac{\lambda}{n}\right)^2 \frac{F}{w_0^2} \cdot \xi \tag{B6}$$

with the wavelength λ, the refractive index $n \approx n_{\mathrm{diamond}}$ for a mostly diamond-filled cavity, the cavity quality factor Q, the mode volume V_m, and the electric field dipole overlap $\xi = \cos^2\theta = 1/3$. Here, we also use the two relations $V_m = (\pi w_0^2 d)/4$ and $Q = 2d/\lambda F$ to replace V_m and Q by the finesse F and the mode waist w_0.

The finesse is measured as $F = 12\,000$ with an uncertainty of 10% when averaging over many consecutive measurements of the cavity linewidth and free spectral range. The mode waist is simulated (compare Ref. [63]) to be $w_0 = 1.35$ μm with an uncertainty of 10% using the fiber radius of curvature and the cavity length, both measured. Evaluating the Purcell factor for the given numerical values yields a distribution that is shown in Fig. 8 with $F_{\mathrm{P}} = 28^{+10}_{-4}$. The measured value $F_{\mathrm{P,ideal}} = 36 \pm 11$ is in the range of expected Purcell factors for perfect spatial and spectral overlap.

As soon as we deviate from the ideal scenario where the ensemble is spatially and spectrally spread over the entire cavity mode—thus reducing the spectral and spatial cavity-emitter overlap—we expect the Purcell factor to drop. However, we measure $F_{\mathrm{P,ideal}}$ via a power-dependent set of $g^{(2)}$ functions where the $g^{(2)}$ contributions of individual emitters scale quadratically with their respective radiation rate and, thus, also quadratically with the individual Purcell factor. Thus, the drop of F_{P} when leaving the ideal scenario

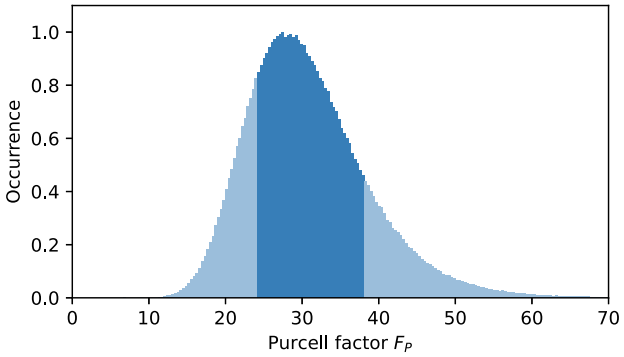

FIG. 8. Distribution of expected Purcell factors for the experimentally determined parameters. The highlighted area shows the 1σ confidence interval.

is not as dramatic as one would naively expect. Because of this experimental bias toward high Purcell factors, we do not see a significant deviation from the scenario of perfect spectral and spatial mode overlap.

APPENDIX C: THEORETICAL MODEL

We take into account the branching ratio into the ZPL $\zeta = 0.03$ and account for the different dipole orientations $\xi = \cos^2\theta = 1/3$ and their different locations in the cavity mode with an effectively reduced coupling

$$g = \sqrt{\frac{3\pi c^3 \gamma}{2\omega^2 V_m}\zeta\xi} \propto \sqrt{\zeta\xi}, \tag{C1}$$

with the mode volume V_m. We expect that the emission comprises two orthogonal linear polarizations and, thus, two independent subensembles, which couple with equal strength to two orthogonal cavity polarization modes. We motivate the use of a model with just three optical transitions of the same polarization, develop more sophisticated models, and compare them to the present simplifications in a related theoretical work [44].

For the system with multiple NV subensembles, the dynamics is described by the QME:

$$\frac{\partial}{\partial t}\hat{\rho} = -\frac{i}{\hbar}\left[\hat{H}_{\rm tls} + \hat{H}_{\rm c} + \hat{H}_{\rm tls-c}, \hat{\rho}\right] - \kappa\mathcal{D}[\hat{a}]\hat{\rho} - \sum_{k=1}^{N_{\rm ene}}\sum_{i=1}^{N_k}\left\{\eta_k\mathcal{D}[\hat{\sigma}_{k,i}^{+}]\hat{\rho} + \gamma_k\mathcal{D}[\hat{\sigma}_{k,i}^{-}]\hat{\rho} + \frac{\chi_k}{2}\mathcal{D}[\hat{\sigma}_{k,i}^{z}]\hat{\rho}\right\}. \tag{C2}$$

The Hamiltonian $\hat{H}_{\rm tls} = \hbar\sum_{k=1}^{N_{\rm ene}}(\omega_k/2)\sum_{i=1}^{N_k}\hat{\sigma}_{k,i}^{z}$ describes the NV centers as two-level systems with the transition frequency ω_k and the Pauli operator $\hat{\sigma}_{k,i}^{z}$, where the labels k and i indicate the individual subensemble and the individual NV center, respectively. The Hamiltonian $\hat{H}_c = \hbar\omega_c\hat{a}^{+}\hat{a}$ describes the optical cavity with frequency ω_c, the photon creation $\hat{a}^{+}$, and annihilation operators $\hat{a}$. The Hamiltonian $\hat{H}_{\rm tls-c} = \hbar\sum_{k=1}^{N_{\rm ene}} g_k\sum_{i=1}^{N_k}\{\hat{\sigma}_{k,i}^{+}\hat{a} + \hat{a}^{+}\hat{\sigma}_{k,i}^{-}\}$ describes the NV-optical cavity coupling with a strength g_k and the raising and lowering operators $\hat{\sigma}_{k,i}^{+}$, $\hat{\sigma}_{k,i}^{-}$. The Lindblad terms describe the cavity photon loss, the individual decay, pure dephasing, and pumping of the two-level systems with rates κ, γ_k, χ_k, and η_k, respectively, and the superoperator is defined as $\mathcal{D}[\hat{o}]\hat{\rho} = \frac{1}{2}\{\hat{o}^{+}\hat{o}, \hat{\rho}\} - \hat{o}\,\hat{\rho}\,\hat{o}^{+}$ (for any operator $\hat{o}$). The second-order autocorrelation function can be computed with the expression $g^{(2)}(\tau) = \langle\hat{a}^{+}(t_{ss})\hat{a}^{+}(t_{ss}+\tau)\hat{a}^{-}(t_{ss}+\tau)\hat{a}^{-}(t_{ss})\rangle/\langle\hat{a}^{+}(t_{ss})\hat{a}^{-}(t_{ss})\rangle$, where t_{ss} refers to the time for the system reaching steady state. The numerator can be transformed into the expression $\mathrm{tr}\{\hat{a}^{+}\hat{a}^{-}\hat{\varrho}(\tau)\}$ in the Schrödinger picture, where the ancillary operator $\hat{\varrho}(\tau)$ satisfies also the QME as $\hat{\rho}(\tau)$ with, however, the initial condition $\hat{\varrho}(0) = \hat{a}^{-}\hat{\rho}(t_{ss})\hat{a}^{+}$ according to quantum regression theorem.

To describe the ideal system with identical NV centers, we remove the label k in the above model and further eliminate adiabatically the optical cavity to achieve an effective master equation, which differs from the original one by replacing $\hat{H}_c + \hat{H}_{\rm tls-c}$ with $\hat{H}_{\rm shift} = \hbar(\delta\omega/2)\sum_{i=1}^{N}\hat{\sigma}_i^{z}$, and $\kappa\mathcal{D}[\hat{a}]\hat{\rho}$ with $\Gamma\mathcal{D}[\sum_{i=1}^{N}\hat{\sigma}_i^{-}]\hat{\rho}$, where $\delta\omega = 2g^2(\omega_c-\omega_0)/[(\omega_c-\omega_0)^2 + ((\kappa+\eta+\gamma)/2+\chi)^2]$ and $\Gamma = g^2\kappa/[(\omega_c-\omega_0)^2 + ((\kappa+\eta+\gamma)/2+\chi)^2]$ are the cavity-induced frequency shift and Purcell-enhanced decay rate, respectively. To proceed, we introduce the collective operators $\hat{J}_x = \frac{1}{2}\sum_{i=1}^{N}(\hat{\sigma}_i^{-}+\hat{\sigma}_i^{+})$, $\hat{J}_y = (i/2)\sum_{i=1}^{N}(\hat{\sigma}_i^{-}-\hat{\sigma}_i^{+})$, $\hat{J}_z = \frac{1}{2}\sum_{i=1}^{N}\hat{\sigma}_i^{z}$, and $\hat{J}^2 = \sum_{i=x,y,z}(\hat{J}_i)^2$ and define the Dicke states from the eigenvalue problems $\hat{J}^2|J,M\rangle = J(J+1)|J,M\rangle$ and $\hat{J}_z|J,M\rangle = M|J,M\rangle$. By expressing the Dicke states for N two-level systems as the product states of $N-1$ two-level systems and one two-level system (using the Clebsch-Gordan coefficients), one can identify the dissipative effects in the collective Dicke state picture induced by the incoherent pumping, decay, and dephasing of individual two-level systems [27,28] [Fig. 1(e)]. In this way, we can derive and then solve the equation for the density matrix elements $\rho_{\rm MM'}^{J}(t)$ within the Dicke states space (the density matrix is diagonal in J). From $\rho_{\rm MM'}^{J}(t)$, we can extract the population of the Dicke states $P_{\rm JM}(t) = \rho_{\rm MM}^{J}(t)$, the radiation rate $I_{\rm rad}(t) = \Gamma\langle\hat{J}^{+}\hat{J}^{-}\rangle(t) = \Gamma\sum_{\rm J,M}|A_{\rm JM}^{-}|^2 P_{\rm JM}(t)$, and the second-order autocorrelation function $g^{(2)}(\tau) = \langle\hat{J}^{+}(t_{\rm ss})\hat{J}^{+}(t_{\rm ss}+\tau)\hat{J}^{-}(t_{\rm ss}+\tau)\hat{J}^{-}(t_{\rm ss})\rangle/[I_{\rm rad}(t_{\rm ss})/\Gamma]^2$, where the numerator can be calculated in a similar way as stated in the previous paragraph. In Sec. S1 of Supplemental Material [34], we provide the corresponding codes based on the QUTIP package [43].

For the system with multiple NV subensembles, we adopt a second-order mean-field approach to derive the equation $(\partial/\partial t)\langle\hat{o}\rangle = \mathrm{tr}\{\hat{o}[(\partial/\partial t)\hat{\rho}]\}$ for the mean value $\langle\hat{o}\rangle = \mathrm{tr}\{\hat{o}\,\hat{\rho}\}$ from the QME, apply the approximation $\langle\hat{o}\,\hat{p}\,\hat{q}\rangle \approx \langle\hat{o}\rangle\langle\hat{p}\,\hat{q}\rangle + \langle\hat{p}\rangle\langle\hat{o}\,\hat{q}\rangle + \langle\hat{q}\rangle\langle\hat{o}\,\hat{p}\rangle - 2\langle\hat{o}\rangle\langle\hat{p}\rangle\langle\hat{q}\rangle$ to

truncate the equation hierarchy to obtain a closed set of equations, and assume the NV centers in each subensemble to be identical. Furthermore, we consider the equations at the steady state and derive the semianalytical expressions for the intracavity photon number $\langle \hat{a}^\dagger \hat{a} \rangle \approx i \sum_{k=1}^{N_{\mathrm{ene}}} (N_k g_k/\kappa)(\langle \hat{\sigma}_{ki}^+ \hat{a} \rangle - \langle \hat{a}^\dagger \hat{\sigma}_{ki}^+ \rangle)$, the population differences $\langle \sigma_{ki}^z \rangle \approx [-2ig_k(\langle \sigma_{ki}^+ \hat{a} \rangle - \langle \hat{a}^\dagger \sigma_{ki}^+ \rangle) + \eta_k - \gamma_k]/(\gamma_k + \eta_k)$, and the NV-NV correlations $\langle \sigma_{ki}^+ \sigma_{k'i'}^- \rangle \approx (\omega_k^* - \omega_{k'})^{-1}(g_k \langle \sigma_{ki}^z \rangle \langle \sigma_{k'i'}^+ \hat{a} \rangle^* - g_{k'} \langle \sigma_{k'i'}^z \rangle \langle \sigma_{ki}^+ \hat{a} \rangle)$ and the NV-photon correlations $\langle \sigma_{ki}^+ \hat{a} \rangle \approx (\omega_{ki}^* - \omega_c)^{-1}[g_k(\langle \hat{a}^\dagger \hat{a} \rangle \langle \sigma_{ki}^z \rangle - \langle \sigma_{ki}^+ \sigma_{ki'}^- \rangle) + \sum_{k' \neq k}^{N_{\mathrm{ene}}} N_{k'} g_{k'} \langle \sigma_{ki}^+ \sigma_{k'i'}^- \rangle + (g_k/2)(\langle \sigma_{ki}^z \rangle + 1)]$. By taking the complex conjugate of the last equation, we can also obtain the expressions for $\langle \hat{a}^\dagger \sigma_{ki}^+ \rangle$. In these expressions, the complex frequencies are defined as $\omega_k = \omega_k - i(\gamma_k + \eta_k) + \chi_k$ and $\omega_c = \omega_c - i\kappa/2$. In practice, we insert the first three expressions into the last one and then solve the self-consistent equations for the NV-photon correlations with the FindRoot command in Mathematica; see the codes in Sec. S1 of Supplemental Material [34].

[1] R. H. Dicke, *Coherence in spontaneous radiation processes*, Phys. Rev. **93**, 99 (1954).

[2] N. Skribanowitz, I. P. Herman, J. C. MacGillivray, and M. S. Feld, *Observation of Dicke superradiance in optically pumped HF gas*, Phys. Rev. Lett. **30**, 309 (1973).

[3] A. V. Andreev, V. I. Emel'yanov, and Y. A. Il'inskiĭ, *Collective spontaneous emission (Dicke superradiance)*, Sov. Phys. Usp. **23**, 493 (1980).

[4] M. Gross and S. Haroche, *Superradiance: An essay on the theory of collective spontaneous emission*, Phys. Rep. **93**, 301 (1982).

[5] J. M. Raimond, P. Goy, M. Gross, C. Fabre, and S. Haroche, *Statistics of millimeter-wave photons emitted by a Rydberg-atom maser: An experimental study of fluctuations in single-mode superradiance*, Phys. Rev. Lett. **49**, 1924 (1982).

[6] M. O. Scully and A. A. Svidzinsky, *The super of superradiance*, Science **325**, 1510 (2009).

[7] K. Cong, Q. Z., Y. Wang, G. T. Noe, A. Belyanin, and J. Kono, *Dicke superradiance in solids*, J. Opt. Soc. Am. B **33**, C80 (2016).

[8] G. Raino, M. A. Becker, M. I. Bodnarchuk, R. F. Mahrt, M. V. Kovalenko, and T. Stöferle, *Superfluorescence from lead halide perovskite quantum dot superlattices*, Nature (London) **563**, 671 (2018).

[9] J. Q. Grim, A. S. Bracker, M. Zalalutdinov, S. G. Carter, A. C. Kozen, M. Kim, C. S. Kim, J. T. Mlack, M. Yakes, B. Lee, and Dl Gammon, *Scalable in operando strain tuning in nanophotonic waveguides enabling three-quantum-dot superradiance*, Nat. Mater. **18**, 963 (2019).

[10] D. Meiser, J. Ye, D. R. Carlson, and M. J. Holland, *Prospects for a millihertz-linewidth laser*, Phys. Rev. Lett. **102**, 163601 (2009).

[11] J. G. Bohnet, Z. Chen, J. M. Weiner, D. Meiser, M. J. Holland, and J. K. Thompson, *A steady-state superradiant laser with less than one intracavity photon*, Nature (London) **484**, 78 (2012).

[12] G. Ferioli, A. Glicenstein, L. Henriet, I. Ferrier-Barbut, and A. Browaeys, *Storage and release of subradiant excitations in a dense atomic cloud*, Phys. Rev. X **11**, 021031 (2021).

[13] Z. Shen and A. Dogariu, *Subradiant directional memory in cooperative scattering*, Nat. Photonics **16**, 148 (2022).

[14] M. Lei, R. Fukumori, J. Rochman, B. Zhu, M. Endres, J. Choi, and A. Faraon, *Many-body cavity quantum electrodynamics with driven inhomogeneous emitters*, Nature (London) **617**, 271 (2023).

[15] A. Rastogi, E. Saglamyurek, T. Hrushevskyi, and L. J. LeBlanc, *Superradiance-mediated photon storage for broadband quantum memory*, Phys. Rev. Lett. **129**, 120502 (2022).

[16] V. Paulisch, M. Perarnau-Llobet, A. González-Tudela, and J. I. Cirac, *Quantum metrology with one-dimensional superradiant photonic states*, Phys. Rev. A **99**, 043807 (2019).

[17] R. Bonifacio, P. Schwendimann, and Fritz Haake, *Quantum statistical theory of superradiance. I*, Phys. Rev. A **4**, 302 (1971).

[18] R. Bonifacio and L. A. Lugiato, *Cooperative radiation processes in two-level systems: Superfluorescence*, Phys. Rev. A **11**, 1507 (1975).

[19] G. Davies, *The Jahn-Teller effect and vibronic coupling at deep levels in diamond*, Rep. Prog. Phys. **44**, 787 (1981).

[20] Ph. Tamarat, T. Gaebel, J. R. Rabeau, M. Khan, A. D. Greentree, H. Wilson, L. C. L. Hollenberg, S. Prawer, P. Hemmer, F. Jelezko, and J. Wrachtrup, *Stark shift control of single optical centers in diamond*, Phys. Rev. Lett. **97**, 083002 (2006).

[21] J. Wolters, N. Sadzak, A. W. Schell, T. Schröder, and O. Benson, *Measurement of the ultrafast spectral diffusion of the optical transition of nitrogen vacancy centers in nano-size diamond using correlation interferometry*, Phys. Rev. Lett. **110**, 027401 (2013).

[22] C. Bradac, M. T. Johnsson, M. van Breugel, B. Q. Baragiola, R. Martin, M. L. Juan, G. K. Brennen, and T. Volz, *Room-temperature spontaneous superradiance from single diamond nanocrystals*, Nat. Commun. **8**, 1205 (2017).

[23] A. Auffèves, D. Gerace, S. Portolan, A. Drezet, and M. F. Santos, *Few emitters in a cavity: From cooperative emission to individualization*, New J. Phys. **13**, 093020 (2011).

[24] H. A. M. Leymann, A. Foerster, F. Jahnke, J. Wiersig, and C. Gies, *Sub- and superradiance in nanolasers*, Phys. Rev. Appl. **4**, 044018 (2015).

[25] E. M. Purcell, H. C. Torrey, and R. V. Pound, *Resonance absorption by nuclear magnetic moments in a solid*, Phys. Rev. **69**, 37 (1946).

[26] T. Grange, G. Hornecker, D. Hunger, J.-P. Poizat, J.-M. Gérard, Pascale Senellart, and A. Auffèves, *Cavity-funneled generation of indistinguishable single photons from strongly dissipative quantum emitters*, Phys. Rev. Lett. **114**, 193601 (2015).

[27] Yuan Zhang, Yu-Xiang Zhang, and Klaus Mølmer, *Monte-Carlo simulations of superradiant lasing*, New J. Phys. **20**, 112001 (2018).

[28] N. Shammah, S. Ahmed, N. Lambert, S. de Liberato, and F. Nori, *Open quantum systems with local and collective*

incoherent processes: Efficient numerical simulations using permutational invariance, Phys. Rev. A **98**, 063815 (2018).

[29] D. Bhatti, J. von Zanthier, and G. Agarwal, *Superbunching and nonclassicality as new hallmarks of superradiance*, Sci. Rep. **5**, 17335 (2015).

[30] M. Hennrich, A. Kuhn, and G. Rempe, *Transition from antibunching to bunching in cavity QED*, Phys. Rev. Lett. **94**, 053604 (2005).

[31] J. Wiersig, C. Gies, F. Jahnke, M. Aßmann, T. Berstermann, M. Bayer, C. Kistner, S. Reitzenstein, C. Schneider, S. Höfling, A. Forchel, C. Kruse, J. Kalden, and D. Hommel, *Direct observation of correlations between individual photon emission events of a microcavity laser*, Nature (London) **460**, 245 (2009).

[32] F. Jahnke, C. Gies, M. Aßmann, M. Bayer, H. a. M. Leymann, A. Foerster, J. Wiersig, C. Schneider, M. Kamp, and S. Höfling, *Giant photon bunching, superradiant pulse emission and excitation trapping in quantum-dot nanolasers*, Nat. Commun. **7**, 11540 (2016).

[33] E. Janitz, M. Ruf, M Dimock, A. Bourassa, J. Sankey, and L. Childress, *Fabry-Perot microcavity for diamond-based photonics*, Phys. Rev. A **92**, 043844 (2015).

[34] See Supplemental Material at http://link.aps.org/supplemental/10.1103/PhysRevX.14.041055 for numerical codes and additional theoretical results.

[35] M. Radtke, E. Bernardi, A. Slablab, R. Nelz, and E. Neu, *Nanoscale sensing based on nitrogen vacancy centers in single crystal diamond and nanodiamonds: Achievements and challenges*, Nano Futures **3**, 042004 (2019).

[36] Maryam Zahedian, Jietian Liu, Ricardo Vidrio, Shimon Kolkowitz, and Jennifer T. Choy, *Modeling of radiative emission from shallow color centers in single crystalline diamond*, Laser Photonics Rev. **17**, 2200529 (2023).

[37] Andrei Faraon, Paul E. Barclay, Charles Santori, Kai-Mei C. Fu, and Raymond G. Beausoleil, *Resonant enhancement of the zero-phonon emission from a colour centre in a diamond cavity*, Nat. Photonics **5**, 301 (2011).

[38] C. Gies, J. Wiersig, M. Lorke, and F. Jahnke, *Semiconductor model for quantum-dot-based microcavity lasers*, Phys. Rev. A **75**, 013803 (2007).

[39] Kai-Mei C. Fu, Charles Santori, Paul E. Barclay, Lachlan J. Rogers, Neil B. Manson, and Raymond G. Beausoleil, *Observation of the dynamic Jahn-Teller effect in the excited states of nitrogen-vacancy centers in diamond*, Phys. Rev. Lett. **103**, 256404 (2009).

[40] V. V. Temnov and U. Woggon, *Photon statistics in the cooperative spontaneous emission*, Opt. Express **17**, 5774 (2009).

[41] A. Bychek, Ch. Hotter, D. Plankensteiner, and H. Ritsch, *Superradiant lasing in inhomogeneously broadened ensembles with spatially varying coupling*, Open Res. Eur. **1**, 73 (2021).

[42] Q. Wu, Y. Zhang, X. Yang, S.-L. Su, C. Shan, and K. Mølmer, *A superradiant maser with nitrogen-vacancy center spins*, Sci. Chin. Phys. Mech. Astron. **65**, 217311 (2021).

[43] B. Julsgaard and K. Mølmer, *Dynamical evolution of an inverted spin ensemble in a cavity: Inhomogeneous broadening as a stabilizing mechanism*, Phys. Rev. A **86**, 063810 (2012).

[44] Y.-D. Qu, Y. Zhang, P. Ni, C. Shan, D. Hunger, and K. Mølmer, *Superradiance from nitrogen vacancy centers coupled to an ultranarrow optical cavity*, arXiv:2407.09755v1.

[45] K. Debnath, Y. Zhang, and K. Mølmer, *Collective dynamics of inhomogeneously broadened emitters coupled to an optical cavity with narrow linewidth*, Phys. Rev. A **100**, 053821 (2019).

[46] C. Sánchez Muñoz, E. del Valle, A. González Tudela, K. Müller, S. Lichtmannecker, M. Kaniber, C. Tejedor, J. J. Finley, and F. P. Laussy, *Emitters of N-photon bundles*, Nat. Photonics **8**, 550 (2014).

[47] A. C. Santos, A. Cidrim, C. J. Villas-Boas, R. Kaiser, and R. Bachelard, *Generating long-lived entangled states with free-space collective spontaneous emission*, Phys. Rev. A **105**, 053715 (2022).

[48] A. Roulet and C. Bruder, *Quantum synchronization and entanglement generation*, Phys. Rev. Lett. **121**, 063601 (2018).

[49] D. Braun, G. Adesso, D. Benatti, R. Floreanini, U. Marzolino, M. W. Mitchell, and S. Pirandola, *Quantum-enhanced measurement without entanglement*, Rev. Mod. Phys. **90**, 035006 (2018).

[50] M. Koppenhöfer, P. Groszkowski, H.-K. Lau, and A. A. Clerk, *Dissipative superradiant spin amplifier for enhanced quantum sensing*, PRX Quantum **3**, 030330 (2022).

[51] J. Wiercinski, E. M. Gauger, and M. Cygorek, *Phonon coupling versus pure dephasing in the photon statistics of cooperative emitters*, Phys. Rev. Res. **5**, 013176 (2023).

[52] J.-H. Kim, S. Aghaeimeibodi, C. J. K. Richardson, R. O. Leavitt, and E. Waks, *Super-radiant emission from quantum dots in a nanophotonic waveguide*, Nano Lett. **18**, 4734 (2018).

[53] R. E. Evans, M. K. Bhaskar, D. D. Sukachev, C. T. Nguyen, A. Sipahigil, M. J. Burek, B. Machielse, G. H. Zhang, A. S. Zibrov, E. Bielejec, H. Park, M. Lončar, and M. D. Lukin, *Photon-mediated interactions between quantum emitters in a diamond nanocavity*, Science **362**, 662 (2018).

[54] D. M. Lukin, M. A. Guidry, J. Yang, M Ghezellou, S. D. Mishra, H. Abe, T. Ohshima, J. Ul-Hassan, and J. Vučkovic, *Two-emitter multimode cavity quantum electrodynamics in thin-film silicon carbide photonics*, Phys. Rev. X **13**, 011005 (2023).

[55] R. Reimann, W. Alt, T. Kampschulte, T. Macha, L. Ratschbacher, N. Thau, S. Yoon, and D. Meschede, *Cavity-modified collective Rayleigh scattering of two atoms*, Phys. Rev. Lett. **114**, 023601 (2015).

[56] J. Heupel, M. Pallmann, J. Körber, R. Merz, M. Kopnarski, R. Stöhr, J. P. Reithmaier, D. Hunger, and C. Popov, *Fabrication and characterization of single-crystal diamond membranes for quantum photonics with tunable microcavities*, Micromachines **11**, 1080 (2020).

[57] M. Pallmann, T. Eichhorn, J. Benedikter, B. Casabone, T. Hümmer, and D. Hunger, *A highly stable and fully tunable open microcavity platform at cryogenic temperatures*, APL Photonics **8**, 046107 (2023).

[58] D. Hunger, T. Steinmetz, Y. Colombe, C. Deutsch, T. W. Hänsch, and J. Reichel, *A fiber Fabry-Perot cavity with high finesse*, New J. Phys. **12**, 065038 (2010).

[59] J. Körber, M. Pallmann, J. Heupel, R. Stöhr, E. Vasilenko, T. Hümmer, L. Kohler, C. Popov, and D. Hunger, *Scanning cavity microscopy of a single-crystal diamond membrane*, Phys. Rev. Appl. **19**, 064057 (2023).

[60] R. Brouri, A. Beveratos, J. Poizat, and P. Grangier, *Photon antibunching in the fluorescence of individual color centers in diamond*, Opt. Lett. **25**, 1294 (2000).

[61] C. Kurtsiefer, S. Mayer, P. Zarda, and H. Weinfurter, *Stable solid-state source of single photons*, Phys. Rev. Lett. **85**, 290 (2000).

[62] M. Fox, *Quantum Optics, an Introduction* (Oxford University, New York, 2006).

[63] S. B. van Dam, M. Ruf, and R. Hanson, *Optimal design of diamond-air microcavities for quantum networks using an analytical approach*, New J. Phys. **20**, 115004 (2018).

Correction: The second and third affiliations were presented in the incorrect order and have been interchanged. An affiliation for the last author was missing and has been added as the sixth affiliation. The omission of a contact author footnote for the third author has been rectified.